












The Radial Variation of the Solar Wind Turbulence Spectra near the Kinetic Break Scale from Parker Solar Probe Measurements

S. Lotz^{1,2,11}, A. E. Nel^{1,11} , R. T. Wicks^{3,11} , O. W. Roberts⁴ , N. E. Engelbrecht^{5,6} , R. D. Strauss^{5,6} , G. J. J. Botha³ ,
E. P. Kontar⁷ , A. Pitňa⁸ , and S. D. Bale^{9,10} 

¹South African National Space Agency, Hermanus, 7200, South Africa

²MUST, Faculty of Engineering, North-West University, South Africa

³Department of Mathematics, Physics and Electrical Engineering, Northumbria University, Newcastle upon Tyne NE1 8ST, UK

⁴Space Research Institute, Austrian Academy of Sciences, Schmiedlstrasse 6, Graz, A-8042, Austria

⁵Center for Space Research, North-West University, Potchefstroom, 2522, South Africa; dutoit.strauss@nwu.ac.za

⁶National Institute for Theoretical and Computational Sciences (NITheCS), South Africa

⁷School of Physics and Astronomy, University of Glasgow, Glasgow G12 8QQ, UK

⁸Department of Surface and Plasma Science, Faculty of Mathematics and Physics, Charles University, V Holešovičkách 2, 180 00 Prague, Czech Republic

⁹Physics Department, University of California, Berkeley, CA 94720-7300, USA

¹⁰Space Sciences Laboratory, University of California, Berkeley, CA 94720-7450, USA

Received 2022 October 3; revised 2022 November 16; accepted 2022 December 4; published 2023 January 17

Abstract

In this study we examine the radial dependence of the inertial and dissipation range indices, as well as the spectral break separating the inertial and dissipation range in power density spectra of interplanetary magnetic field fluctuations using Parker Solar Probe data from the fifth solar encounter between ~ 0.1 and ~ 0.7 au. The derived break wavenumber compares reasonably well with previous estimates at larger radial distances and is consistent with gyro-resonant damping of Alfvénic fluctuations by thermal protons. We find that the inertial scale power-law index varies between approximately -1.65 and -1.45 . This is consistent with either the Kolmogorov ($-5/3$) or Iroshnikov–Kraichnan ($-3/2$) values, and has a very weak radial dependence with a possible hint that the spectrum becomes steeper closer to the Sun. The dissipation range power-law index, however, has a clear dependence on radial distance (and turbulence age), decreasing from -3 near 0.7 au (4 days) to $-4 [\pm 0.3]$ at 0.1 au (0.75 days) closer to the Sun.

Unified Astronomy Thesaurus concepts: [Space plasmas \(1544\)](#); [Solar wind \(1534\)](#); [Interplanetary turbulence \(830\)](#)

1. Introduction

High-cadence magnetic field observations made by the Parker Solar Probe (PSP) during its various perihelia provide us with an unprecedented opportunity to study the radial evolution of various quantities associated with the dissipation of solar wind turbulence (see, e.g., Woodham et al. 2019; Perrone et al. 2020; Alexandrova et al. 2021; Chhiber et al. 2021a), motivated by the fact that a greater understanding of the processes of kinetic dissipation in magnetized plasma is essential for explaining the physical origin and evolution of the solar wind (e.g., Bruno & Carbone 2016; Duan et al. 2020; Matteini et al. 2020; Telloni et al. 2021; Zhao et al. 2022a). This, in turn, also informs modeling efforts of turbulence transport (e.g., Engelbrecht & Strauss 2018; Chhiber et al. 2019; Adhikari et al. 2020, 2021a) and energetic particle transport (e.g., Strauss et al. 2017; Engelbrecht 2019; Laitinen & Dalla 2019; Chhiber et al. 2021b) and relates to density turbulence that is important for solar radio burst interpretation (e.g., Krupar et al. 2020; Kontar et al. 2019). Magnetic field fluctuations in the solar wind are commonly observed to follow a power-law spectrum. The inertial range is created by an energy-conserving spectral cascade (e.g., Smith et al. 2006) where interactions between fluctuations can still be described

by fluid dynamics (however, for an exception, see Bian et al. 2010). The spectral index in the inertial range has been observed to be close to both the Kolmogorov (1941) value of $-5/3$, as well as the Iroshnikov–Kraichnan value of $-3/2$ (see, e.g., Smith et al. 2006; Podesta 2011; Chen et al. 2020; Zhao et al. 2020). This range is followed by a break and then a steepening in the magnetic field power spectrum, where the MHD description breaks down and kinetic effects of individual particles, and thermal heating, start playing a role (Alexandrova et al. 2008). The dissipation range spectral index is dependent on the type of turbulent fluctuation present, being either Alfvén waves or coherent structures, and can vary significantly, ranging between ~ -1 and -4 (Leamon et al. 1998; Markovskii et al. 2006; Smith et al. 2006; Alexandrova 2008; Bruno et al. 2014; Bruno & Trenchi 2014; Lion et al. 2016; Vech et al. 2018; Franci et al. 2020). The physical mechanisms responsible for the break between the inertial and dissipation range at these ion-kinetic scales are still not fully understood (Matteini et al. 2020). The processes at play in energy transport in the transition range and how it affects the properties of plasma is still an open question (e.g., Goldstein et al. 2015; Bruno & Carbone 2016; Terres & Li 2022). The break frequency f_b , where the transition from inertial to dissipation range is observed, has been shown to display a radial dependence in previous studies. Analyzing observations taken in the 0.42 to 5.3 au range during radial alignments respectively between MESSENGER and WIND, and WIND and ULYSSES, Bruno & Trenchi (2014) found that the break frequency increased as the heliocentric distance decreased such that $f_b \propto r^{-1.09 \pm 0.11}$. In another study Duan et al. (2020) used

¹¹ Equal contribution authors.

data from the cruise phase of the second orbit of PSP, ranging from 0.17 to 0.63 au, to measure the spectral break that those authors interpret as the transition to kinetic turbulence. They found that the break frequency increased with a decrease in heliocentric distance, following a power law of $f_b \propto r^{-1.11 \pm 0.01}$.

A wide array of studies examine time periods for the break scale and find evidence for a link to the kinetic plasma physics of protons (e.g., Goldstein et al. 1994; Hamilton et al. 2008; Markovskii et al. 2008; Smith et al. 2012; Chen et al. 2014; Woodham et al. 2018). At 1 au the ion scale spectral break tends to occur near $f \sim 0.1$ –1 Hz in the spacecraft frame (e.g., Leamon et al. 1998; Smith et al. 2001; Bale et al. 2005; Markovskii et al. 2008; Bourouaine et al. 2012). The break is located near the spacecraft frame frequencies that correspond to either the proton gyroradius l_g where damping of kinetic Alfvén waves becomes significant or the proton inertial length l_i where protons decouple from the turbulent magnetic field. It may also be associated with magnetic reconnection via the so-called disruption scale (for more detail see Vech et al. 2018, Terres & Li 2022, and references therein). The break frequency has been observationally associated with these various characteristic plasma length scales, for example Leamon et al. (1998) and Leamon et al. (2000) report from analyses of WIND data that this break occurs at spatial scales in the plasma frame near the proton gyroradius. Alternatively the break may be related to the combined scale $l_i + l_g = 2\pi k_c^{-1}$, which is associated with cyclotron resonance of Alfvén waves propagating along the mean field direction (e.g., Leamon et al. 1998; Bruno & Trenchi 2014; Engelbrecht & Strauss 2018; Woodham et al. 2018). At 1 au it is often the case that plasma $\beta \sim 1$ implying $l_g \sim l_i$, which makes it difficult to determine which of spatial scales is related to the break (see, e.g., Terres & Li 2022). To overcome this limitation, Chen et al. (2014) investigated intervals with extreme values of plasma β where the two scales are well separated. It was found that the break tends to be associated with the larger of the two scales, which is consistent with the break being near the combined scale. Bruno & Trenchi (2014) performed a study of how the spectral break changes with heliocentric distance and found the best agreement to be with the combined scale, with a radial dependence of the wavenumber at which this break occurs of $k_b \propto r^{-1.08 \pm 0.08}$. A study of WIND data also confirmed that the best agreement is with the combined scale (Woodham et al. 2018).

In this work we determine the spectrum near the break wavenumber and spectral indices using high-cadence PSP magnetic field measurements taken during its fifth orbit, in an extension of the study of Duan et al. (2020). The fifth orbit includes observations from 2020 May 7 to 2020 June 19, with PSP radial distance from the Sun varying between 0.1 and 0.7 au. These values are then compared to the theoretical estimates for this quantity by employing in situ observations for the various plasma quantities they are a function of in an attempt to determine which is the dominant turbulence dissipation process in the inner heliosphere. The break wavenumber is then quantitatively compared to previous studies and the radial dependence across the widest range of heliocentric distances yet measured is calculated. Furthermore, the radial evolution of the inertial and dissipation range spectral indices are also investigated. The next section details the analysis method employed in this study. Sections 3 and 4 present the results of this study with regard to the dissipation

range onset frequency/wavenumber, and spectral indices, respectively. Finally, the results are discussed in Section 5.

2. Data Analysis

PSP is a three-axis-stabilized Sun-pointing spacecraft in an elliptical heliocentric orbit, with aphelia between Earth and Venus (Whittlesey et al. 2020). The Solar Wind Electrons, Alphas, and Protons (SWEAP) instrument suite on board the PSP primarily measures solar wind thermal plasma. The suite consists of three electrostatic analyzer instruments, called the Solar Probe ANalyzers (SPANs): a Sun-pointing Faraday Cup (SPC) that primarily measures protons, alpha particles, and periodically electrons and the Solar Probe Analyzers (SPAN) that are situated at either side of the spacecraft bus and measures protons, alpha particles, heavy ions (SPAN-Ion), and electrons (SPAN-Electron). We use density and thermal speed data from SPC and temperature from the SPAN-Ion instrument. These instruments were designed to overlap their fields of view and capabilities, and make complementary measurements (Kasper 2021). We restricted the analysis to periods when data quality (quantified by the quality flag parameters) was at its highest level for the SPAN, SPC, and fluxgate magnetometer (MAG) instruments. The three-component heliocentric (R , T , and N where R is in the radial direction, T is perpendicular to R and lying in the equatorial plane, and N is normal to this plane and completes the right-handed coordinate system) solar wind magnetic field is measured by the MAG fluxgate magnetometer from the FIELDS instrument (Bale et al. 2016). During this period the spacecraft moved, in terms of radial distance, between ~ 0.1 and 0.7 au. Figure 1 shows, from top to bottom, the magnetic field magnitude, the solar wind proton density, the effective temperature, and the solar wind speed against radial distance for the inward and the outward part of the orbit; note the logarithmic y-axis necessary to capture the wide change in parameters over the orbit in the top three panels.

The magnetic field is observed at data rate d quantified by samples per instrument cycle. For this study we only utilized intervals with data rate $d \geq 64$ samples / cycle. The instrument cycle duration is $L \approx 0.874$ s (Bale et al. 2016), i.e., $d = 64$ would translate to 55 samples per second. The time between samplings is not always consistent and to rectify this we interpolate the B time series data to a fixed rate of L/d . We estimate the break frequency in the magnetic field spectra (f_b) using a procedure similar to the method employed by Woodham et al. (2019). The time series spanning 44 days is divided into non-overlapping windows of 128 s each, and f_b is estimated for each of these windows. The approximately 1025 hr of orbit 5 equates to roughly 28,000 128 s intervals; however, only a fraction of these intervals results in reliable f_b estimates. The f_b estimation procedure is illustrated in Figure 2 for one such interval.

For every 128 s interval of $\mathbf{B} = [B_R, B_T, B_N]$ ($N \times 3$ matrix with N the number of magnetic field observations) the power spectral density of \mathbf{B} is computed by taking the trace $P(f) = \text{tr}\{\mathbf{P}(f)\}$ of the matrix $\mathbf{P}(f) = \hat{\mathbf{B}}(f)\hat{\mathbf{B}}(f)^*$, where $\hat{\mathbf{B}}(f)$ denotes the Fourier components of \mathbf{B} at frequency f and $\hat{\mathbf{B}}(f)^*$ its complex conjugate. Since the shape of the spectral break is more pronounced in log space than linear space we linearly interpolate the power terms along log-spaced frequencies, denoted by $P_l(f_l)$. This is the blue dotted curve in Figure 2. Overlapping linear fits are applied to $P_l(f_l)$ and the average slope and intercept are determined within the inertial and dissipation ranges (green and red shaded regions in Figure 2).

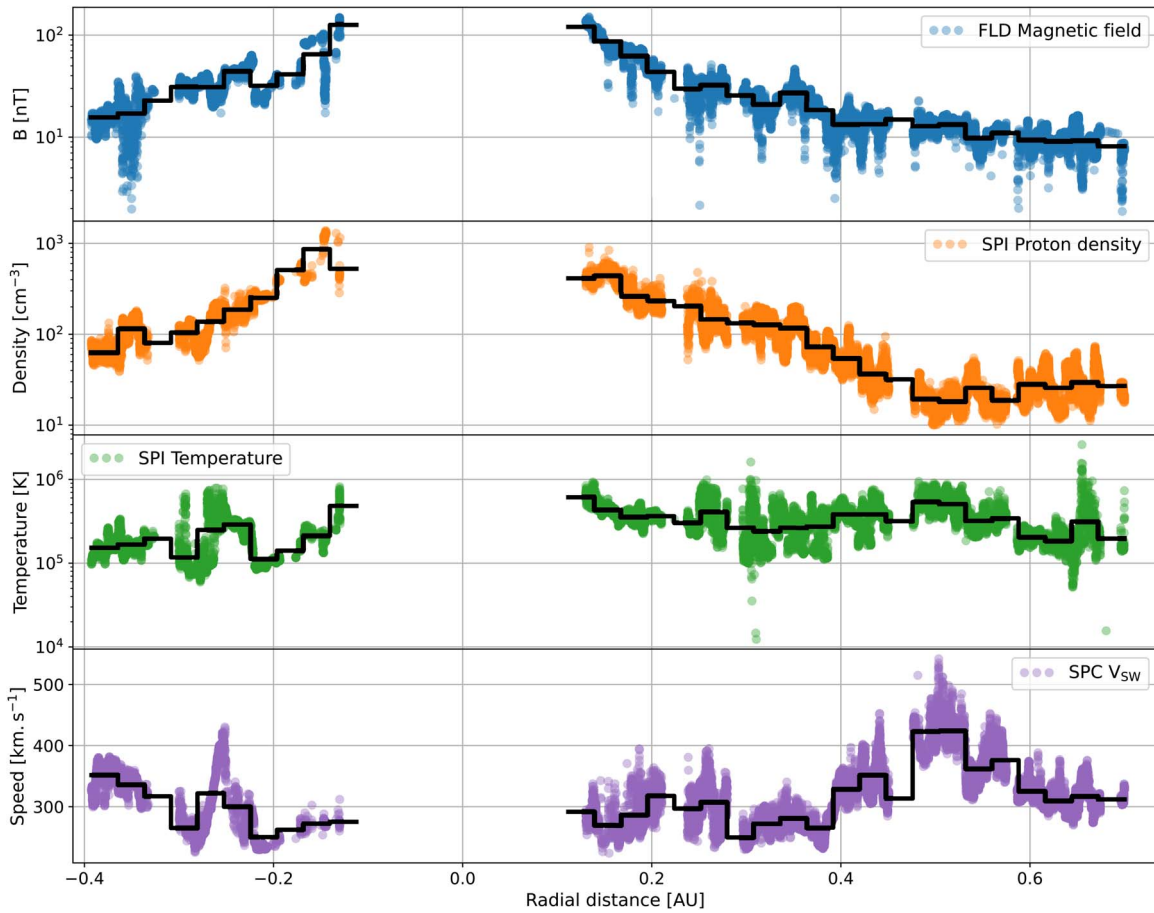


Figure 1. An overview of the solar wind plasma measurements during PSP orbit 5. The black stepped curves indicate the local mean for 50 equispaced radial distance bins.

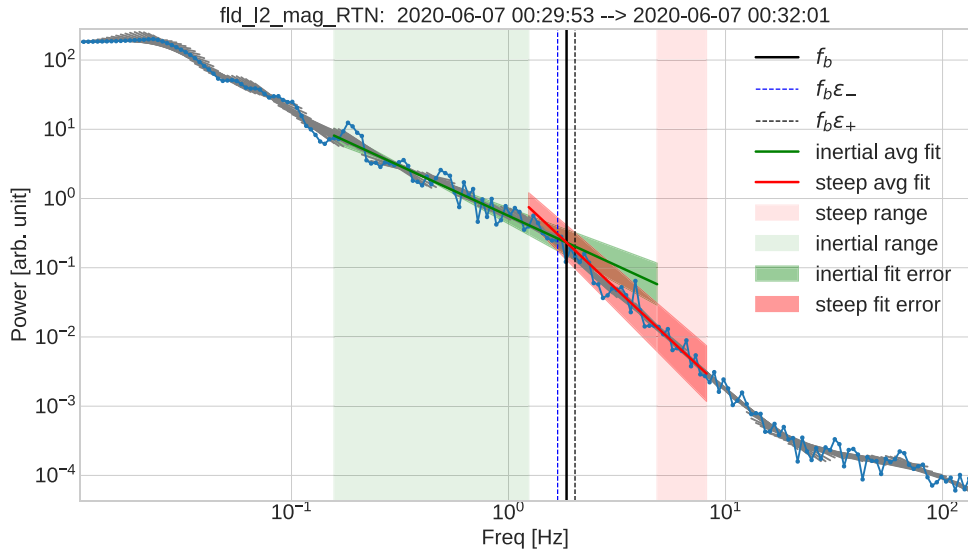


Figure 2. Magnetic field spectrum from a solar wind interval measured by PSP. Blue dotted line: initial spectrum. Gray lines: individual slopes measured over 20 points, and used to determine the (1) green slope, which is the average fit for the inertial range, and (2) red slope, which is the average fit for the dissipation range. The vertical black line represents the break frequency approximation. The green highlighted section defines the cutoff for the inertial range estimation and the red-highlighted section the cutoff for the dissipation range estimation.

These average fits are indicated by the red and green lines and their intersection determines the break frequency estimate f_b (black vertical dashed line in Figure 2). The mean standard deviation of the linear fits are used to estimate the uncertainty,

denoted by the shaded regions around the average linear fits. We define the uncertainty in the f_b estimate as the frequencies where the upper and lower bounds of the linear fit uncertainty regions overlap (see Figure 2).

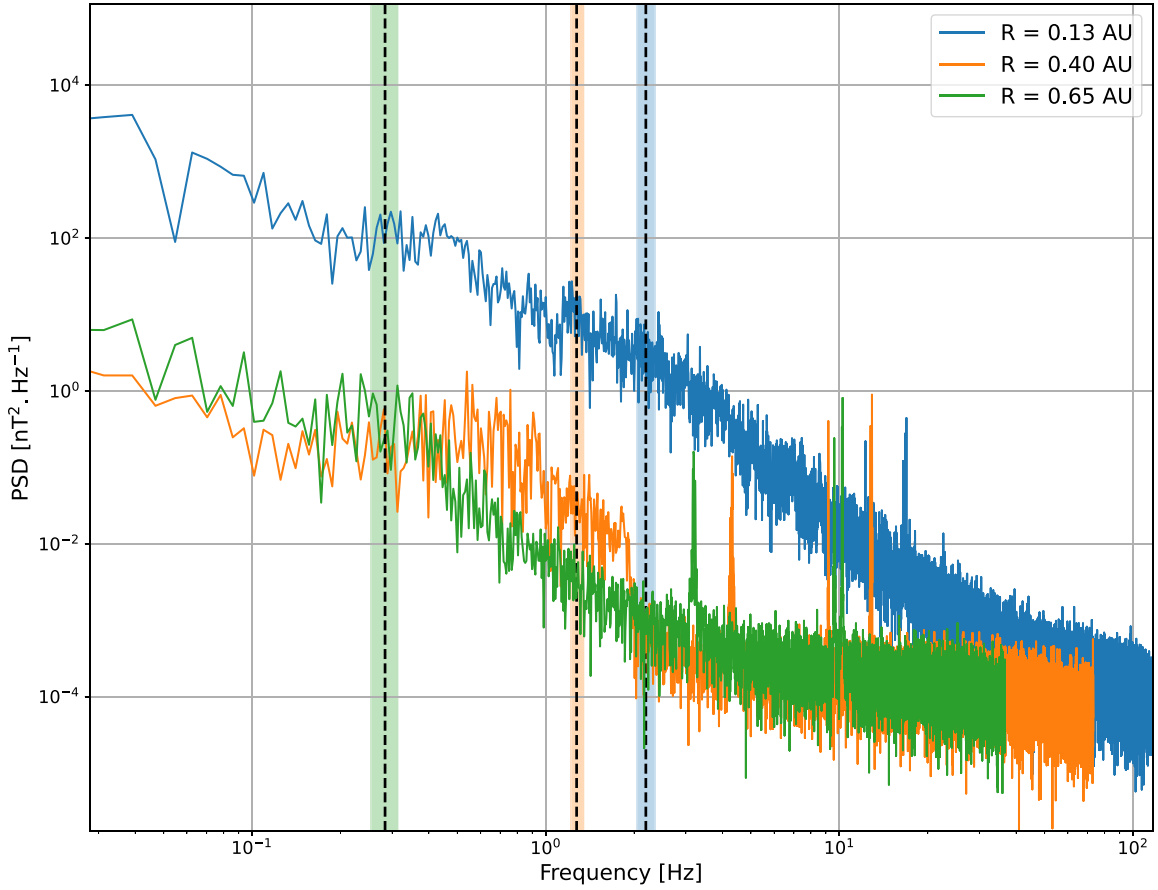


Figure 3. Power spectral distributions at different heliocentric distances. The blue spectrum is from an interval measured at 0.13 au, the orange spectrum from 0.4 au, and the green spectrum as measured at 0.65 au. Vertical dashed lines indicate the estimated break frequency for each spectrum and the shaded regions the error estimate.

This yields a set of 26,581 estimates of f_b along with an upper and lower uncertainty ($f_b\epsilon^-$, $f_b\epsilon^+$) for the orbit 5 data set. The uncertainty estimates allow us to discard problematic f_b estimates. All estimates with (i) $f_b\epsilon^- > f_b\epsilon^+$, or (ii) f_b outside the range of frequencies in the signal, or (iii) $f_b\epsilon^-$ or $f_b\epsilon^+$ beyond the dissipation and inertial ranges are discarded. This results in a final set of 8551 reliable estimates of f_b . From the estimated break frequency, and the measured solar wind speed in each interval, a corresponding wavenumber is calculated as

$$k_b = \frac{2\pi f_b}{V_{sw}}, \quad (1)$$

with associated break scale $l_d = 2\pi/k_b$. As such, the Taylor hypothesis is explicitly used in this study. For turbulence analyses performed on observations taken specifically near the Alfvén critical point, this could be problematic (see, e.g., Bourouaine & Perez 2018, 2019, 2020). In terms of the dispersive regime specifically, Howes et al. (2014) report that such a regime, were it primarily supported by Whistler waves, would violate Taylor’s hypothesis, while Klein et al. (2014) expect a flattening of the dissipation range due to this issue. Note also that we do not take the angle between the flow and magnetic fields into account (Bourouaine et al. 2012; Chen et al. 2014; Duan et al. 2018).

In order to compare our results with the various proposed break wavenumbers, these quantities are calculated directly from PSP observations.

As a first approach, temperature isotropy ($T_{\text{eff}} = T_{\parallel} = T_{\perp}$) is assumed, allowing the effective plasma proton temperature to be calculated from the equipartition theorem as $mu_{\text{eff}}^2 = 3kT_{\text{eff}}$, where u_{eff} is the effective thermal speed. From this, the proton gyroscale can be estimated as

$$l_g = 2\pi \frac{u_{\text{eff}}}{\Omega_{ci}} = \frac{2\pi}{k_g}, \quad (2)$$

with $\Omega_{ci} = qB/m_i$ the proton gyro-frequency. The proton inertial length now follows as

$$l_i = 2\pi \frac{c}{\omega_{ci}} = 2\pi \frac{V_A}{\Omega_{ci}} = \frac{2\pi}{k_i}, \quad (3)$$

with $V_A = B/\sqrt{\mu_0 n_i m_i}$ the Alfvén speed. Thermal particles can also resonate with circularly polarized waves when, in the guiding center frame, the following resonance condition is met

$$\omega^* = n\Omega^*, \quad (4)$$

where ω^* is the wave frequency, Ω^* the particle cyclotron frequency, and $n = \pm 1$ labels left-handed and right-handed waves, respectively. Transforming back to the bulk flow frame, the resonance condition becomes

$$\omega - \mathbf{k} \cdot \mathbf{v} = n\Omega. \quad (5)$$

Assuming left-hand, parallel propagating Alfvén waves with $\omega^2 = k_{\parallel}^2 V_A^2$, resonating with thermal protons, Doppler shifted by their (parallel) thermal speeds u_{eff} , one obtains the so-called

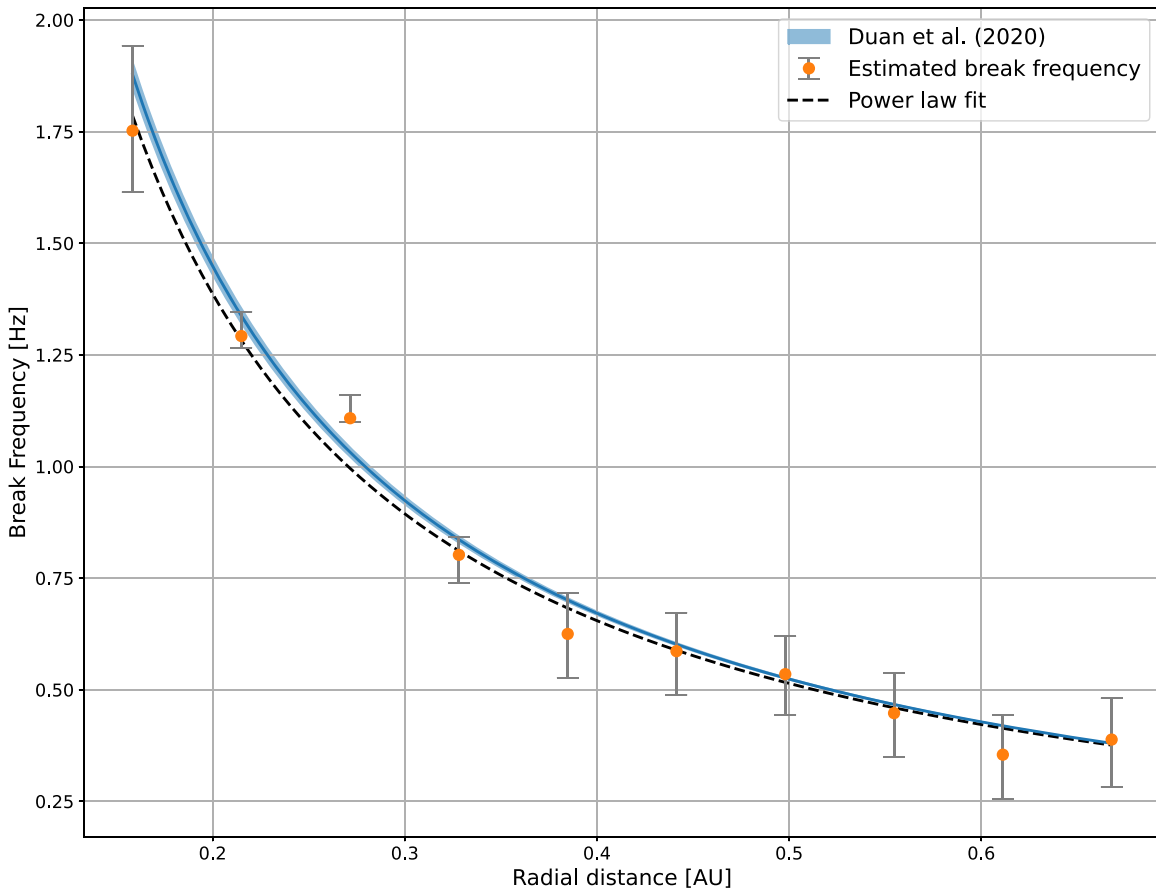


Figure 4. Break frequency, as a function of radial distance, compared with the Duan et al. (2020) power-law estimate ($f_b \propto r^{-1.11 \pm 0.01}$) determined from PSP data in the range 0.17–0.63 au. The dashed line shows a power-law fit to our results ($f_b \propto r^{-1.08 \pm 0.04}$).

proton cyclotron resonance as (see, e.g., Engelbrecht & Strauss 2018, and references therein)

$$k_c = \frac{\Omega_{ci}}{V_A + u_{\text{eff}}} = \frac{2\pi}{l_g + l_i}. \quad (6)$$

The following sections outline the results of the analyses discussed above.

3. Dissipation Range Break Frequency and Onset Wavenumber

Figure 3 shows the magnetic field spectral densities at three different heliocentric distances, 0.13, 0.40, and 0.67 au. The dashed vertical lines represent the estimated break frequency and its estimated error is indicated by the shaded band for each of these examples. Sharp peaks in power spectral densities at frequencies above 1 Hz are visible in all of the traces. These are caused by the spacecraft attitude control system and change in amplitude and frequency slowly over time. The increase in total power of the fluctuations and break frequency toward the Sun is expected. This behavior can also be seen over wider radial distance in Figure 4, showing binned estimates of the break frequency as a function of radial distance. A power-law fit to the data is indicated by a black dashed line ($f_b \propto r^{-1.08 \pm 0.04}$). This agrees reasonably well with the fit performed by Duan et al. (2020), shown in blue ($f_b \propto r^{-1.11 \pm 0.01}$).

The wavenumbers change with radial distance and we show this in Figure 5. The set of k_b estimates are divided into five bins, depicted by the top panel. Lower panels show the

distribution of k_b for each radial bin. As a function of radial distance, these distributions become steeper further away from the Sun, so that median and mean averages (denoted by short and long dashed lines, respectively) shift further away from distribution peaks at smaller radial distances. Overall, distribution peaks shift toward larger values of k_b as radial distances increase, with a corresponding increase in the median and mean average values for this quantity.

The PSP results presented in this work enables us to extend earlier estimates of wavenumber to smaller radial distances. Figure 6 shows k_b corresponding to the median (blue markers) and mean (red markers) values of the distributions illustrated in Figure 5. The green markers correspond to earlier results for this quantity reported by Bruno & Trenchi (2014), who employ observations from MESSENGER, WIND, and ULYSSES to calculate values of k_b corresponding to an overall radial range spanning 0.42 and 5.3 au. The units of these data points are here adjusted for comparison with the values acquired in the present analysis. This range overlaps with the range of radial distances considered here and, as can be seen from Figure 6, the break wavenumbers calculated by Bruno & Trenchi (2014) tie in reasonably well with estimates from the present study. An average of the values for k_b reported by Smith et al. (2012) from an analysis of spacecraft observations at 1 au is also shown, and estimates the study of Bruno & Trenchi (2014) fall well within the uncertainty of that value. Not unexpectedly, the radial behavior of the observations shown in Figure 6 suggests a power-law radial dependence for k_b , similar to that seen for the break frequency. Accordingly, the figure also shows a

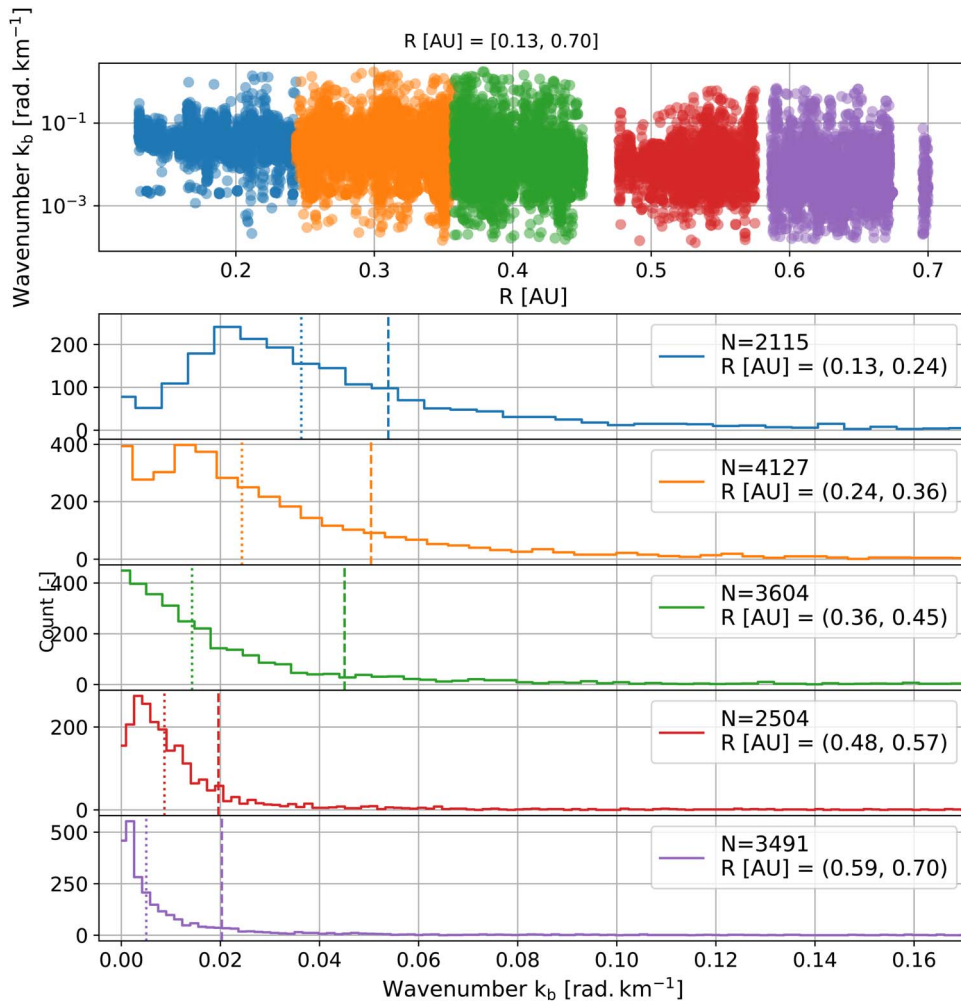


Figure 5. The break scale wavenumber estimations are binned, according to radial heliocentric distance, into five intervals and shown in the top panel, with the wavenumber given in radians per kilometer and radial distance in astronomical units. The corresponding distributions obtained for each respective binned data set are shown in the lower panels as a function of wavenumber. The mean (dashed line) and median (dotted line) of each histogram is indicated by vertical lines.

power-law fit to the observations, with exponent -1.18 ± 0.02 , a value steeper than that reported by Bruno & Trenchi (2014).

In order to directly compare the dissipation range onset wavenumbers calculated here with those wavenumbers corresponding to the various length scales that have been proposed previously, Figure 7 shows k_b as a function of wavenumbers corresponding to the cyclotron resonance scale, the proton gyroscale, and the ion inertial length, as calculated from the corresponding in situ measurements, with corresponding correlation coefficients indicated in the legend. Of all three length scales, the cyclotron resonance wavenumber best fits the dissipation range onset wavenumber calculated here, although the considerable scatter in the data points leads to a relatively coefficient of determination (R^2).

The dashed line in the figure indicates where k_b is equal to the model wavenumber. When using the cyclotron wavelength model wavenumber for comparison (blue circles), the results follow this trend extremely well.

4. Spectral Indices

In a similar method to that used in the previous section, Figure 8 shows the estimated power-law indices of the inertial and dissipation range turbulence, along with their distributions,

binned into different radial intervals. The median and standard deviation of each binned histogram is calculated and shown in Figure 9 as a function of radial distance. The inertial range index distribution does not show a change in width, and remains relatively constant with an increase in radial distance. The dissipation range index shows a constant distribution width, and generally decreases as radial distances get larger. This is shown more explicitly in Figure 9, where both spectral indices, with their accompanying uncertainties, are shown as a function of the average radial distances corresponding to the bins for which they were calculated. The inertial range spectral indices appear to remain relatively constant as a function of radial distance (within uncertainty). Furthermore, it is not clear whether either the Kolmogorov or Iroshnikov–Kraichnan values for this quantity, indicated respectively by the black and red lines on the figure, are favored, once more due to the range of uncertainty. Although this result is similar to the inertial range spectral indices calculated for the fifth and seventh PSP orbits calculated by Zhao et al. (2022b), there are some differences, as the averaged indices reported by those authors steepen from a value roughly between the Iroshnikov–Kraichnan and Kolmogorov values, to a value approximately equal to the Kolmogorov index beyond ~ 0.35 au for the fifth orbit data (see also Sioulas et al. 2022).

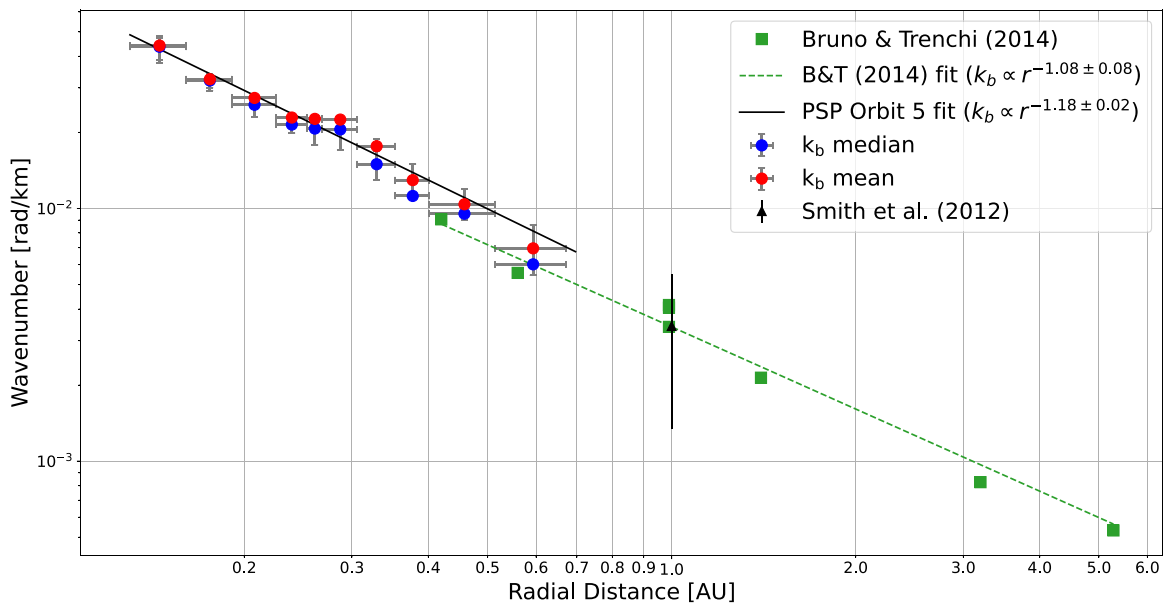


Figure 6. The estimated break scale wavenumber k_b , in radians per kilometer, vs. the radial distance for 10 intervals ranging from 0.1 to 0.7 au. The red markers represent the mean k_b values, and the blue markers the median k_b values. The vertical error bars indicate the error derived from the break frequency estimates. Horizontal error bars indicate the radial range covered. Comparison is made with k_b reported by Bruno & Trenchi (2014) for radial distances 0.42–5.3 au (green squares), as well as the average value for this quantity reported at 1 au by Smith et al. (2012; black triangle), where the error bar indicates the standard deviation of the Smith et al. (2012) measurements.

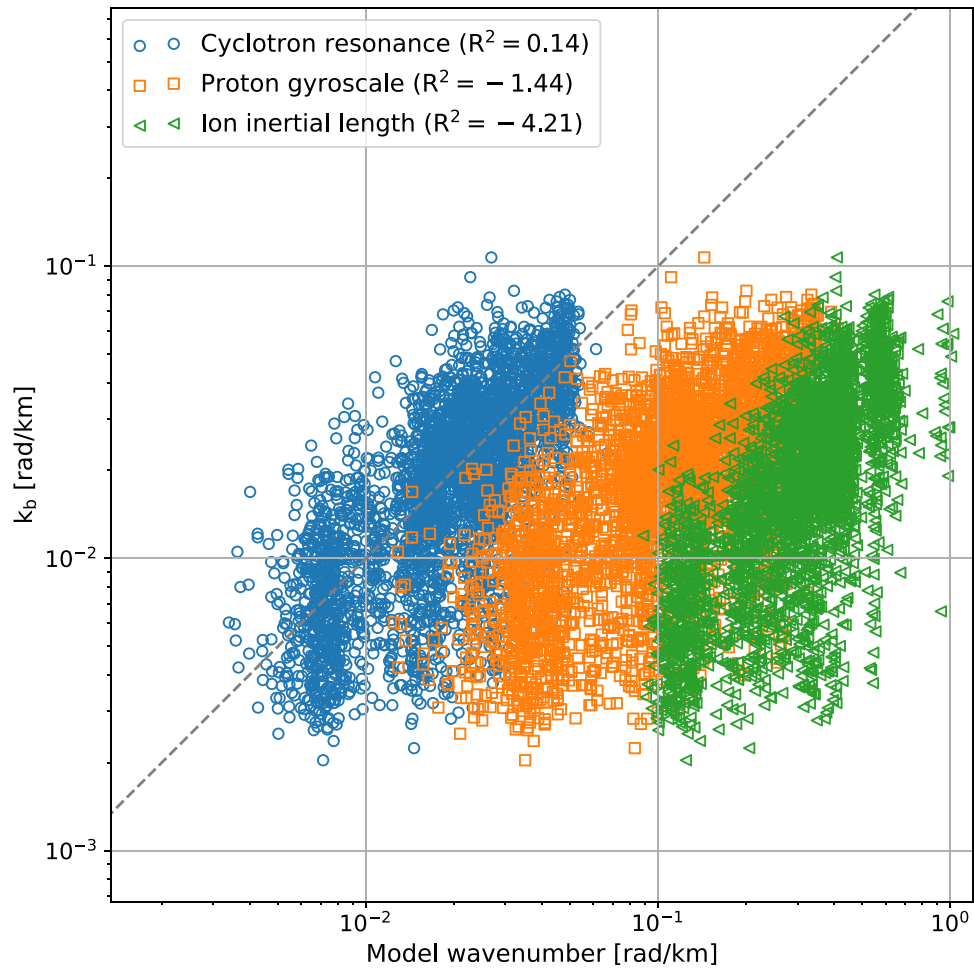


Figure 7. The estimated break scale wavenumber k_b , and a function of the corresponding scale size, calculated from Equations (2)–(6), using in situ observed plasma data. The dashed line indicates perfect linear correlation with a slope of unity and going through the origin; the coefficient of determination R^2 between k_b and the modeled wavenumbers are indicated in the legend.

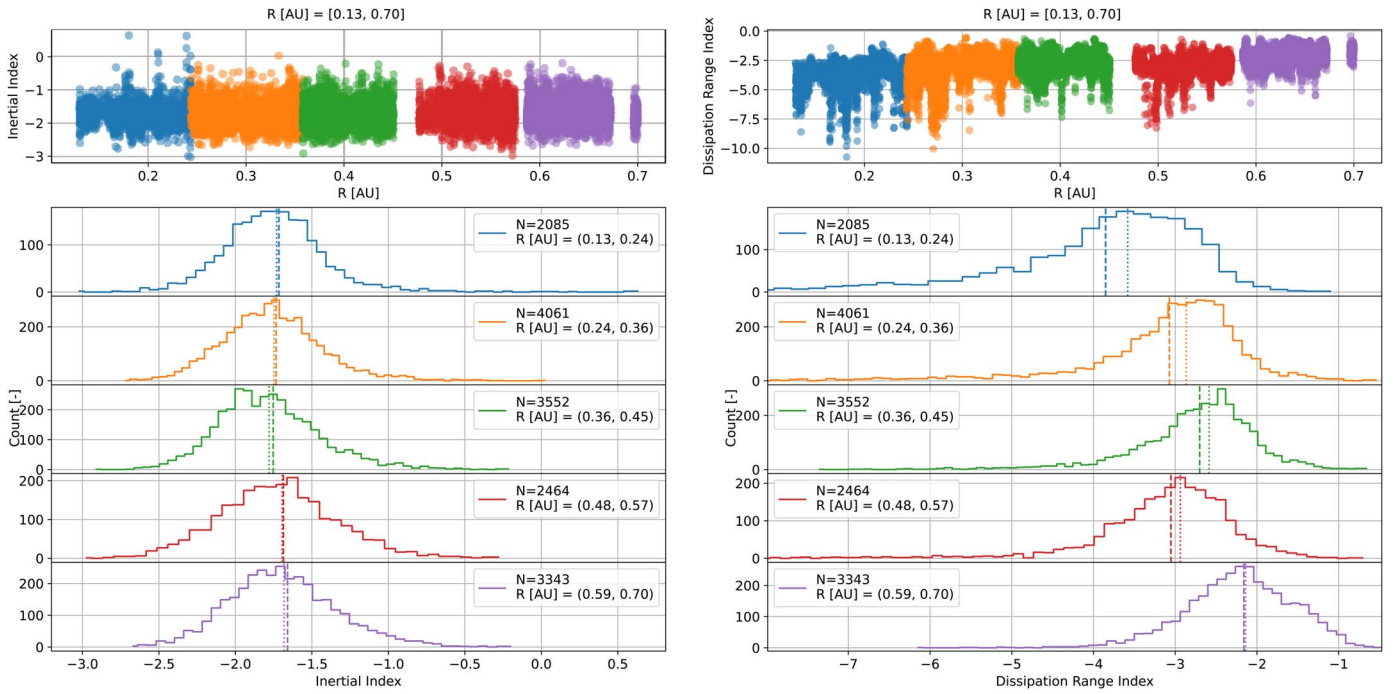


Figure 8. Similar to Figure 5, but now the value of the inertial range power-law index (left column) and dissipation range power-law index (right column) are binned into several radial intervals.

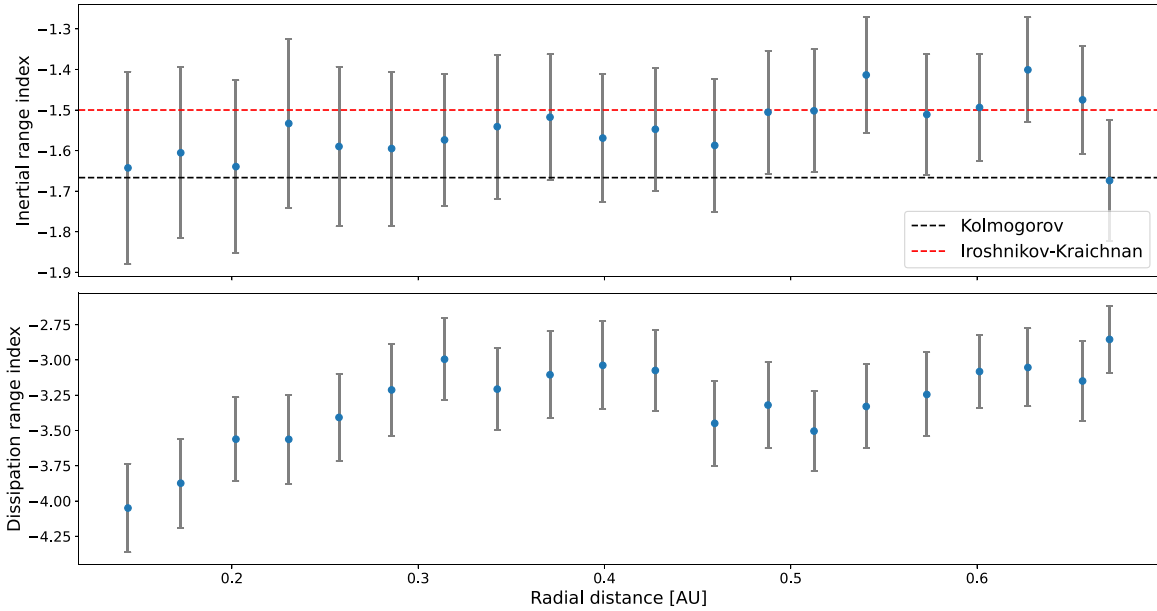


Figure 9. Computed inertial (top) and dissipation range (bottom) power-law indices as a function of radial distance.

Dissipation range spectral indices, however, display a clear radial dependence, increasing in absolute value as radial distance increases, similar to what is reported by Franci et al. (2020). It is interesting to note that, were the violation of the Taylor hypothesis to play a significant role, a flatter dissipation range spectrum would be expected (Klein et al. 2014). The radial behavior of this quantity may be related to the increase in power of the turbulence with decreasing radial distance (see Figure 3), in qualitative agreement with what was reported by Smith et al. (2006) in their analysis of dissipation range spectral indices at 1 au, by Bruno et al. (2014), who found a correlation between steeper dissipation ranges and enhanced turbulence levels, and by Huang et al. (2021) in their analysis of first orbit

PSP data. The radial decrease in the dissipation range spectra index is, however, not uniform, as indicated by the slight drop in this quantity between ~ 0.45 and ~ 0.6 au in Figure 9. This behavior corresponds to a marked increase in the solar wind speed shown in Figure 1, with the implication that the behavior of the dissipation range spectral index at these radial distances may be a reflection of the behavior of this quantity at smaller radial distances due to the fact that the solar wind is “younger” here. To investigate this, the age of the solar wind $\tau = r/V_{sw}$ corresponding to each point in Figure 9 was calculated, and the spectral indices were plotted as a function of this age in Figure 10. The inertial range spectral indices behave in a relatively uniform manner as a function of solar wind age,

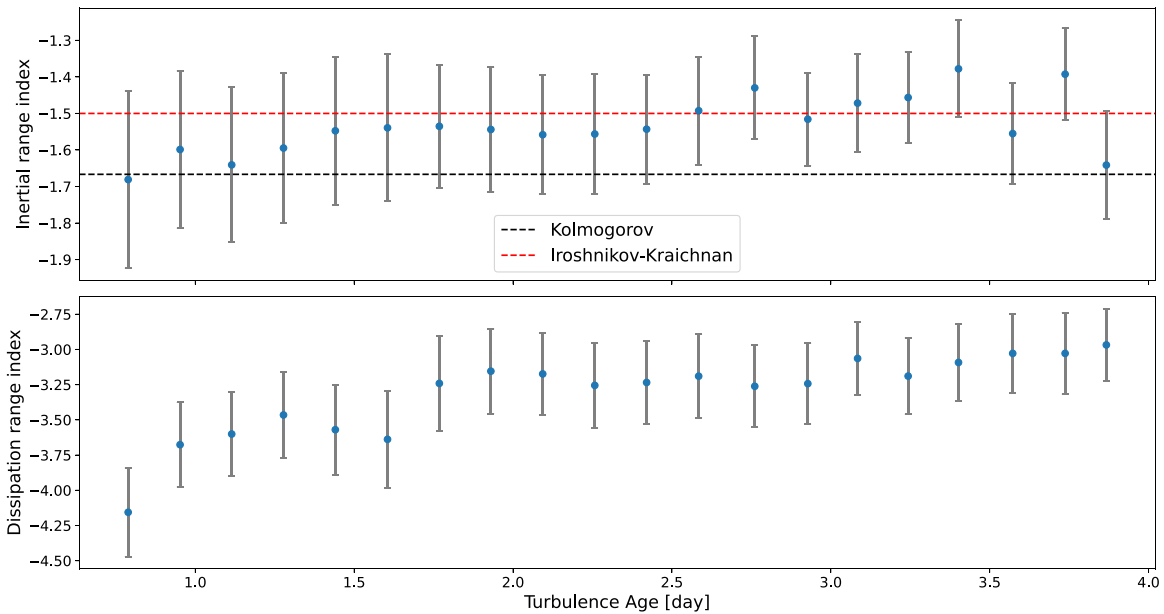


Figure 10. The inertial (top) and dissipation range (bottom) power-law indices as a function of solar wind age.

while the dissipation range spectral indices clearly become steeper as solar wind age decreases.

5. Discussion and Conclusions

This work extends the study of Duan et al. (2020), by considering the radial evolution of the spectral break between the inertial and dissipation ranges of turbulence power spectra calculated for PSP data taken during the fifth perihelion of that spacecraft, as well as the spectral indices associated with these ranges. The radial dependence of the spectral break reported on here closely resembles that found by Duan et al. (2020) for the cruise phase of the second PSP orbit, and ties up with that reported at larger radial distances by Bruno & Trenchi (2014), as well as an average value for this quantity calculated from the results of Smith et al. (2012). We find a radial dependence of $k_b \propto r^{-1.18 \pm 0.02}$. Furthermore, a comparison of the break frequencies calculated here with frequencies corresponding to the proton gyroradius, ion inertial length, and the cyclotron resonance scale, all computed using in situ PSP observations of the various plasma quantities these scales depend on, found that these break frequencies correspond most closely with those corresponding to the cyclotron resonance scale. This finding is in agreement with that of Woodham et al. (2018) in their analysis of WIND data. These results provide a valuable benchmark against which the results of various turbulence transport models (e.g., Engelbrecht & Strauss 2018; Adhikari et al. 2021a) can be tested, as well as a valuable input for solar energetic particle and cosmic-ray transport models.

The present study finds, in contrast to previous studies (e.g., Chen et al. 2020; Shi et al. 2021; Sioulas et al. 2022; Zhao et al. 2022b) that the inertial range spectral index, within uncertainties, remains relatively constant as a function of heliocentric radial distance. However, this index does steepen for intervals of greater age, corresponding to relatively slower solar wind speeds. This discrepancy with the results of prior studies may be due to the fact that the present study does not distinguish between intervals of greater or lesser Alfvénicity. The ambiguity in the results presented here may then be due to the fact that that inertial range spectral indices have been

observed to be steeper for intervals of low Alfvénic content (characterized by Sioulas et al. 2022 as intervals of low normalized cross-helicity), and vice versa (see also Shi et al. 2021). However, the steepening of inertial range spectral indices reported here for older turbulence intervals does agree with the findings of Sioulas et al. (2022), who report such a steepening for slow solar wind intervals.

The dissipation range spectral indices reported on here show a clear radial dependence, becoming less steep at larger radial distances, in agreement with previous studies (e.g., Franci et al. 2020). This could be related to the increase in turbulence levels closer to the Sun (e.g., Adhikari et al. 2021b; Zank et al. 2021 and references therein), and would be in accordance with a correlation between enhanced turbulence levels at 1 au and steeper dissipation range spectral indices reported by Smith et al. (2006). It is interesting to note that, when intervals are binned according to the age of the turbulence, dissipation range spectral indices almost uniformly decrease as radial distance increases.




Another possibility for the mechanism that steepens the dissipation range spectral index is the presence of ion cyclotron waves (ICWs). Bowen et al. (2020) showed that the number, amplitude and duration of ICW packets increases closer to the Sun. The presence of ICWs causes a bump in the spectrum at the proton cyclotron resonance scale (Lion et al. 2016; Wicks et al. 2016; Woodham et al. 2018; Telloni et al. 2019) and so can appear as a steepening of the dissipation range spectrum. Our method rejects spectra with large standard deviation of the fitted lines and so spectra with large peaks due to ICWs will be rejected, but we cannot rule out that low-amplitude ICW effects on the spectra have not been measured as steepening of the dissipation range.

Future work aims to extend the current analysis in two ways. First, by considering longer data intervals, so as to include a portion of the energy-containing range of the turbulence power spectrum, thereby allowing for the calculation of the inertial range outer scale. This, in turn, will enable us to include the disruption scale (e.g., Terres & Li 2022, and references therein in our comparative analyses). Second, the analysis will be

extended to other PSP perihelia, taking into account various additional factors, such as solar wind speed and plasma- β , that are known from previous studies (e.g., Chen et al. 2014; Wang et al. 2018; Sioulas et al. 2022) to influence the dissipation range spectral break frequency. It should also be noted that the influence of Taylor's hypothesis on results calculated for the dispersive regime should be investigated, in the manner proposed by, e.g., Bourouaine & Perez (2019), in more detail. Future measurements with the MeerKAT radio telescope and the Square Kilometer Array are also planned to get information about solar wind density fluctuations at very small scales inside the Alfvén radius, and thus close the gap between the Sun and $\sim 10 R_{\odot}$.

This work is based on the research supported in part by the National Research Foundation of South Africa (NRF grant Nos. 119424, 120345, 120847, and 137793). Opinions expressed and conclusions arrived at are those of the authors and are not necessarily to be attributed to the NRF. The responsibility of the contents of this work is with the authors. Figures prepared with Matplotlib (Hunter 2007) and certain calculations done with NumPy (Harris et al. 2020). R.T.W. is funded by STFC grant ST/V006320/1. E.P.K. was supported by STFC grant ST/T000422/1. Parker Solar Probe was designed, built, and is now operated by the Johns Hopkins Applied Physics Laboratory as part of NASAs Living with a Star (LWS) program (contract NNN06AA01C). Support from the LWS management and technical team has played a critical role in the success of the Parker Solar Probe mission. Thanks to the FIELDS team for providing data (PI: Stuart D. Bale, UC Berkeley). Thanks to the Solar Wind Electrons, Alphas, and Protons (SWEAP) team for providing data (PI: Justin Kasper, BWX Technologies). Software repository at <https://bitbucket.org/stefansansa/psanalysis/>.

ORCID iDs

A. E. Nel  <https://orcid.org/0000-0001-6917-1105>
 R. T. Wicks  <https://orcid.org/0000-0002-0622-5302>
 O. W. Roberts  <https://orcid.org/0000-0002-3913-1353>
 N. E. Engelbrecht  <https://orcid.org/0000-0003-3659-7956>
 R. D. Strauss  <https://orcid.org/0000-0002-0205-0808>
 G. J. J. Botha  <https://orcid.org/0000-0002-5915-697X>
 E. P. Kontar  <https://orcid.org/0000-0002-8078-0902>
 A. Piña  <https://orcid.org/0000-0001-8913-191X>
 S. D. Bale  <https://orcid.org/0000-0002-1989-3596>

References

Adhikari, L., Zank, G. P., Zhao, L. L., et al. 2020, *ApJS*, 246, 38
 Adhikari, L., Zank, G. P., Zhao, L. L., et al. 2021b, *A&A*, 656, A6
 Adhikari, L., Zank, G. P., Zhao, L. L., Nakanotani, M., & Tasmim, S. 2021a, *A&A*, 650, A16
 Alexandrova, O. 2008, *NPGeo*, 15, 95
 Alexandrova, O., Carbone, V., Veltri, P., & Sorriso-Valvo, L. 2008, *ApJ*, 674, 1153
 Alexandrova, O., Jagarlamudi, V. K., Hellinger, P., et al. 2021, *PhRvE*, 103, 063202
 Bale, S. D., Goetz, K., Harvey, P. R., et al. 2016, *SSRv*, 204, 49
 Bale, S. D., Kellogg, P. J., Mozer, F. S., Horbury, T. S., & Reme, H. 2005, *PhRvL*, 94, 215002
 Bian, N. H., Kontar, E. P., & Brown, J. C. 2010, *A&A*, 519, A114
 Bourouaine, S., Alexandrova, O., Marsch, E., & Maksimovic, M. 2012, *ApJ*, 749, 102

Bourouaine, S., & Perez, J. C. 2018, *ApJL*, 858, L20
 Bourouaine, S., & Perez, J. C. 2019, *ApJL*, 879, L16
 Bourouaine, S., & Perez, J. C. 2020, *ApJL*, 893, L32
 Bowen, T. A., Mallet, A., Huang, J., et al. 2020, *ApJS*, 246, 66
 Bruno, R., & Carbone, V. 2016, *Turbulence in the Solar Wind*, Vol. 928 (Cham: Springer International)
 Bruno, R., & Trenchi, L. 2014, *ApJL*, 787, L24
 Bruno, R., Trenchi, L., & Telloni, D. 2014, *ApJL*, 793, L15
 Chen, C. H. K., Bale, S. D., Bonnell, J. W., et al. 2020, *ApJS*, 246, 53
 Chen, C. H. K., Leung, L., Boldyrev, S., Maruca, B. A., & Bale, S. D. 2014, *GeoRL*, 41, 8081
 Chhiber, R., Matthaues, W. H., Bowen, T. A., & Bale, S. D. 2021a, *ApJL*, 911, L7
 Chhiber, R., Matthaues, W. H., Cohen, C. M. S., et al. 2021b, *A&A*, 650, A26
 Chhiber, R., Usmanov, A. V., Matthaues, W. H., Parashar, T. N., & Goldstein, M. L. 2019, *ApJS*, 242, 12
 Duan, D., Bowen, T. A., Chen, C. H. K., et al. 2020, *ApJS*, 246, 55
 Duan, D., He, J., Pei, Z., et al. 2018, *ApJ*, 865, 89
 Engelbrecht, N. E. 2019, *ApJ*, 880, 60
 Engelbrecht, N. E., & Strauss, R. D. T. 2018, *ApJ*, 856, 159
 Franci, L., Del Sarto, D., Papini, E., et al. 2020, arXiv:2010.05048
 Goldstein, M. L., Roberts, D. A., & Fitch, C. A. 1994, *JGR*, 99, 11519
 Goldstein, M. L., Wicks, R. T., Perri, S., & Sahraoui, F. 2015, *RSPTA*, 373, 20140147
 Hamilton, K., Smith, C. W., Vasquez, B. J., & Leamon, R. J. 2008, *JGRA*, 113, A01106
 Harris, C. R., Millman, K. J., van der Walt, S. J., et al. 2020, *Natur*, 585, 357
 Howes, G. G., Klein, K. G., & TenBarge, J. M. 2014, *ApJ*, 789, 106
 Huang, S. Y., Sahraoui, F., Andres, N., et al. 2021, *ApJL*, 909, L7
 Hunter, J. D. 2007, *CSE*, 9, 90
 Kasper, J. 2021, User guide for Parker Solar Probe SWEAP investigation data products, Smithsonian Astrophysical Observatory in Cambridge, MA, the Space Systems Laboratory at the University of California Berkeley, and the University of Michigan, http://sweap.cfa.harvard.edu/sweap_data_user_guide.pdf
 Klein, K. G., Howes, G. G., & TenBarge, J. M. 2014, *ApJL*, 790, L20
 Kolmogorov, A. 1941, *Akademia Nauk SSSR Doklady*, 30, 301
 Kontar, E. P., Chen, X., Chrysaphi, N., et al. 2019, *ApJ*, 884, 122
 Krupar, V., Szabo, A., Maksimovic, M., et al. 2020, *ApJS*, 246, 57
 Laitinen, T., & Dalla, S. 2019, *ApJ*, 887, 222
 Leamon, R. J., Matthaues, W. H., Smith, C. W., et al. 2000, *ApJ*, 537, 1054
 Leamon, R. J., Smith, C. W., Ness, N. F., Matthaues, W. H., & Wong, H. K. 1998, *JGR*, 103, 4775
 Lion, S., Alexandrova, O., & Zaslavsky, A. 2016, *ApJ*, 824, 47
 Markovskii, S. A., Vasquez, B. J., & Smith, C. W. 2008, *ApJ*, 675, 1576
 Markovskii, S. A., Vasquez, B. J., Smith, C. W., & Hollweg, J. V. 2006, *ApJ*, 639, 1177
 Matteini, L., Franci, L., Alexandrova, O., et al. 2020, *FrASS*, 7, 563075
 Perrone, D., Bruno, R., D'Amicis, R., et al. 2020, *ApJ*, 905, 142
 Podesta, J. J. 2011, *JGRA*, 116, A05101
 Shi, C., Velli, M., Panasenco, O., et al. 2021, *A&A*, 650, A21
 Sioulas, N., Huang, Z., Shi, C., et al. 2022, arXiv:2209.02451
 Smith, C. W., Hamilton, K., Vasquez, B. J., & Leamon, R. J. 2006, *ApJL*, 645, L85
 Smith, C. W., Matthaues, W. H., Zank, G. P., et al. 2001, *JGR*, 106, 8253
 Smith, C. W., Vasquez, B. J., & Hollweg, J. V. 2012, *ApJ*, 745, 8
 Strauss, R. D. T., Dresing, N., & Engelbrecht, N. E. 2017, *ApJ*, 837, 43
 Telloni, D., Carbone, F., Bruno, R., et al. 2019, *ApJL*, 885, L5
 Telloni, D., Sorriso-Valvo, L., Woodham, L. D., et al. 2021, *ApJL*, 912, L21
 Terres, M., & Li, G. 2022, *ApJ*, 924, 53
 Vech, D., Mallet, A., Klein, K. G., & Kasper, J. C. 2018, *ApJL*, 855, L27
 Wang, X., Tu, C., He, J., & Wang, L. 2018, *ApJ*, 857, 136
 Whittlessey, P. L., Larson, D. E., Kasper, C. J., et al. 2020, *ApJS*, 246, 74
 Wicks, R. T., Alexander, R. L., Stevens, M., et al. 2016, *ApJ*, 819, 6
 Woodham, L. D., Wicks, R. T., Verscharen, D., & Owen, C. J. 2018, *ApJ*, 856, 49
 Woodham, L. D., Wicks, R. T., Verscharen, D., et al. 2019, *ApJL*, 884, L53
 Zank, G. P., Zhao, L. L., Adhikari, L., et al. 2021, *PhPI*, 28, 080501
 Zhao, G. Q., Lin, Y., Wang, X. Y., et al. 2022a, *ApJ*, 924, 92
 Zhao, L. L., Zank, G. P., Adhikari, L., et al. 2020, *ApJ*, 898, 113
 Zhao, L. L., Zank, G. P., Adhikari, L., & Nakanotani, M. 2022b, *ApJL*, 924, L5